9 December 2005

Science

Vol. 310 No. 5754
Pages 1569–1724 $10

125 YEARS OF GLOBAL Science

AAAS

Rapid Glacial Erosion at 1.8 Ma Revealed by $^4He/^3He$ Thermochronometry

David L. Shuster,[1]*† Todd A. Ehlers,[2] Margaret E. Rusmore,[3] Kenneth A. Farley[1]

Alpine glaciation and river incision control the topography of mountain ranges, but their relative contributions have been debated for years. Apatite $^4He/^3He$ thermochronometry tightly constrains the timing and rate of glacial erosion within one of the largest valleys in the southern Coast Mountains of British Columbia, Canada. Five proximate samples require accelerated denudation of the Klinaklini Valley initiating 1.8 ± 0.2 million years ago (Ma). At least 2 kilometers of overlying rock were removed from the valley at ≥5 millimeters per year, indicating that glacial valley deepening proceeded ≥6 times as fast as erosion rates before ~1.8 Ma. This intense erosion may be related to a global transition to enhanced climate instability ~1.9 Ma.

The hypotheses that alpine glaciers erode at higher rates than rivers (*1*, *2*) and control mountain topographic relief (*3*, *4*) can be tested if pre- and syn-glacial erosion rates can be measured. Debate over the relative contributions of fluvial and glacial erosion to the development of relief has persisted in part because glacial erosion rates have proven difficult to measure, and because it is not well known when and how fast relief develops. Recent advances in quantifying glacial erosion processes include studies of sediment accumulation rates (*5*), suspended sediment loads (*6*), geochronology (*7*–*9*), and numerical modeling of subglacial processes (*10*–*12*). These studies have led to an apparent discrepancy between erosion rates determined from sediment yields (*5*) (on time scales $<10^3$ years) and erosion rates inferred from low-temperature cooling ages (*8*). The latter are sensitive to mean erosion of mountain ranges over much longer time scales ($>10^6$ years) and usually indicate slower rates of erosion than those determined from sediment yields. A critical evaluation of the long-term consequences of glaciation on topography has been hampered by the lack of data to constrain erosion rates before, and during, past glaciations. We present an application of $^4He/^3He$ thermochronometry (*13*) to compare long-term erosion rates before and during alpine glaciation in the Klinaklini valley of the Coast Mountains, British Columbia.

The thermal field of the uppermost few kilometers of Earth's crust responds to changes in surface topography (*14*). Consequently, the history of mountain relief is recorded by the cooling history of rocks as they approach the surface via denudation. (U-Th)/He ages of apatite provide the most sensitive indicator of such near-surface cooling (*14*). This sensitivity arises from the temperature dependence of helium diffusion: The ^4He concentration in a cooling apatite reflects radiogenic production and diffusive loss integrated along the cooling path from ~80°C, where ^4He retention effectively begins, to ~20°C, where retention is nearly quantitative. The (U-Th)/He age of an entire crystal is usually interpreted as the time elapsed since the apatite crossed the ~70°C isotherm (*15*). However, far more detailed information on the cooling path, essential to resolving the role of glacial incision, potentially resides in the spatial distribution of ^4He within a grain.

In a sample containing a uniform distribution of proton-induced ^3He (*16*), sequentially measured $^4He/^3He$ ratios during stepped-extraction document the spatial distribution of radiogenic ^4He (*17*, *18*). When combined with a (U-Th)/He age and helium diffusion kinetics, the ^4He distribution quantitatively constrains the sample's cooling path (*13*, *19*). We applied this method in the Coast Mountains, which extend for ~1000 km along the western margin of North America and have up to 4 km of topographic relief. Previous thermochronology results suggest that mountain building and exhumation >0.5 mm/year began ~10 Ma in this region (*20*). Although this mountain range was heavily incised by glaciers, the timing and magnitude of glacial erosion are only

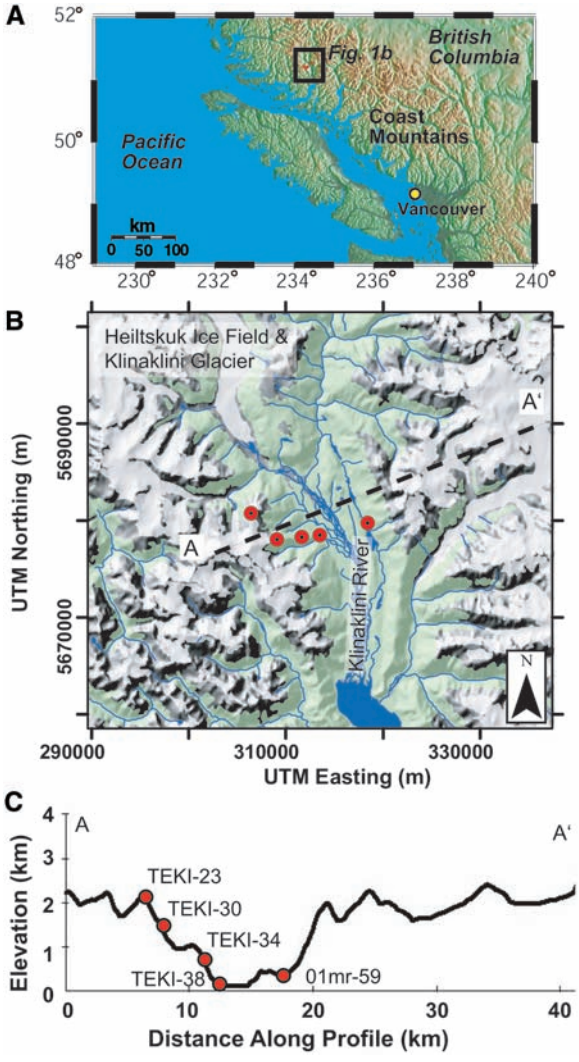

Fig. 1. Topography and sample location maps. (**A**) Regional physiography. Black box represents area shown in (B). (**B**) Shaded relief topography, vegetation cover (green), present-day glacial extent (white to light gray), sample locations (red), and topographic profile location across the Klinaklini valley (A-A′). (**C**) Topographic profile and sample elevations projected onto profile A-A′.

[1]Division of Geological and Planetary Science, California Institute of Technology, 100 23, Pasadena, CA 91125, USA. [2]Department of Geological Sciences, University of Michigan, Ann Arbor, MI 48109, USA. [3]Department of Geology, Occidental College, Los Angeles, CA 90041, USA.

*Present address: Berkeley Geochronology Center, 2455 Ridge Road, Berkeley, CA 94709, USA.
†To whom correspondences should be addressed at Berkeley Geochronology Center, 2455 Ridge Road, Berkeley, CA 94709, USA. E-mail: dshuster@bgc.org

poorly known (*9*, *20*, *21*). We report ^{4}He/^{3}He thermochronometry results for five apatite samples separated from granitic rocks collected along an approximately vertical transect in the ~2.5-km-deep, U-shaped Klinaklini valley (Fig. 1). This valley is one of many similarly shaped glacial valleys and fjords draining the western side of the southern Coast Mountains. Samples were collected 10 km downstream from the confluence of the present-day Heiltskuk Icefield and Klinaklini glacier (~800 km^2) and a former alpine ice sheet of equal or greater size present in the main Klinaklini river valley during the last glacial maximum (*22*) (Fig. 1). From our observations of glacial trim lines, we estimate maximum ice thicknesses of ~2.5 km at this location.

The (U-Th)/He ages of the five samples range from 1.7 to 6.4 Ma. Sample 01MR-59, collected near the Klinaklini valley floor, has the youngest (U-Th)/He age (1.7 ± 0.1 Ma), so its ^{4}He distribution constrains recent thermal perturbations with the highest resolution. Figure 2 is an example of the ^{4}He/^{3}He thermochronometry results for this sample. Details of the other four samples are presented in (*18*) and discussed later. Collectively, these results quantify the helium diffusion kinetics and reveal the spatial distribution of ^{4}He within each sample.

Using the diffusion kinetics quantified from Fig. 2A (*23*), Fig. 2B shows three model cooling paths that produce the (U-Th)/He age observed for sample 01MR-59, yet different spatial distributions of ^{4}He (Fig. 2C). Ejection of α particles from the outer ~20 μm of a mineral confers a predictable shape to the radiogenic ^{4}He distribution, which is independent of diffusion (*13*, *24*). The ^{4}He distribution inferred from the data shown in Fig. 2C is almost entirely explained by α-ejection, contains little diffusive signal (red curve), and requires rapid cooling. In contrast, the ^{4}He/^{3}He measurements clearly preclude thermal histories involving monotonic cooling below 80°C throughout the Pleistocene (green curve).

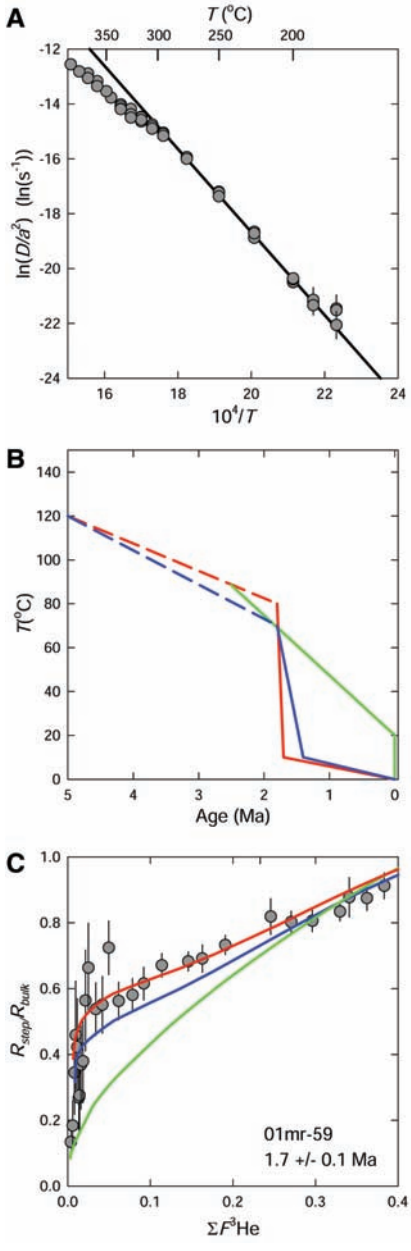

Fig. 2. ^{4}He/^{3}He thermochronometry for apatite sample 01MR-59. (**A**) ^{3}He diffusion Arrhenius plot; circles are the diffusion coefficients, *D*, normalized to the diffusive length scale, *a*, calculated (*38*) from release fractions of proton-induced ^{3}He (*16*). Solid black line is the inferred helium diffusion kinetics for 01MR-59 used to construct models shown in (B) and (C), determined by linear regression to a subset array (includes the 175° to 295°C steps; n = 22). Steps deviate from linearity above 300°C because of a change in diffusion mechanism (*36*), which may not apply to lower temperatures relevant to our models and are therefore excluded from the regression. (**B**) Model cooling paths. Each of these models yields the observed (U-Th)/He age for 01MR-59 (1.7 ± 0.1 Ma). Dashed lines are unconstrained by this sample. (**C**) Ratio evolution diagram. Shown are measured isotope ratios for each release step, R_{step} (R = ^{4}He/^{3}He), normalized to the bulk ratio R_{bulk}, plotted versus the cumulative ^{3}He-release fraction, ΣF^3He. Three models are shown that correspond to the cooling paths in (B). Error bars (1σ) are specified by a vertical line through each point. The best-fitting model is shown in red; the blue curve estimates the minimum cooling rate allowed by the ^{4}He/^{3}He data and provides a confidence limit on the rapid cooling event at 1.8 Ma.

Of the models in Fig. 2, the best fit (red curve) implies that rapid cooling began ~1.8 Ma. Because the ^{4}He/^{3}He data are consistent with an end-member ^{4}He distribution (i.e., no diffusion), they place a stringent restriction on the possible cooling path of the sample. To illustrate this limit, and to estimate a confidence interval for the solution, we sought a lower bound on the cooling rate the sample could have experienced. The blue curve in Fig. 2C shows a lower limit at which point the model is clearly no longer in agreement with the observations, requiring cooling from at least ~70°C at 1.8 Ma to below 20°C by ~1.4 Ma. Therefore, for 01MR-59, the red and blue curves in Fig. 2 define a confidence interval on the cooling path; both demand very rapid cooling denudation beginning 1.8 ± 0.2 Ma.

Widespread gradual climate change to ice-house conditions initiated ~2.7 Ma (*25*), whereas between 1.9 and 1.7 Ma clear evidence exists for a global transition to increased climate variability (*26*), major changes in the provenance of Northern Hemisphere erosion products (*27*, *28*), and the establishment of coldwater upwelling conditions in the tropical and subtropical eastern Pacific ocean (*26*). These global trends in climate are consistent with intense erosion ~1.8 Ma, a time when large ice sheets with a high potential for erosion were likely pervasive across the Coast Mountains and major increases in ice-rafted debris are observed in sea-sediment records (*29*). Thus, glacial erosion within the valley is the most plausible way to explain such rapid cooling of the rocks. Measured geothermal gradients in the region range between ~20° and 30°C/km (*30*, *31*). Assuming these gradients are representative of the thermal field at the time sample 01MR-59 cooled below 80°C, our results imply that ~1700 to 2200 m of overlying rock was rapidly eroded. Adopting the blue curve in Fig. 2B as a lower bound on the cooling rate of 01MR-59, the implied erosion rate was ≥5 mm/year between 1.8 and 1.4 Ma. These results also imply ≤300 m of erosion within the valley since 1.4 Ma.

An erosion event of this magnitude must have affected samples in a broader region, although the magnitude of erosion could be spatially variable. Application of ^{4}He/^{3}He thermochronometry on multiple, neighboring samples provides a test for internal consistency and a way to bootstrap solutions and develop a three-dimensional denudation record through time. For example, assuming that thermal gradients between samples were always ≤30°C/km, a best-fit cooling path for one sample restricts the acceptable cooling path of a second sample located 500 m (vertically) to be offset by no more than 15°C at all times. We tested the internal consistency of our results using a vertical profile of samples collected ~6 km from sample 01MR-59 (Fig. 1).

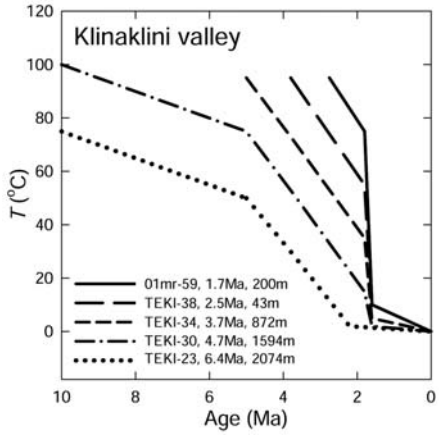

Fig. 3. Internally consistent set of cooling paths for a near-vertical array of samples collected from the west wall of Klinaklini valley. Listed in the legend are the name, (U-Th)/He age, and elevation of each sample, respectively. The corresponding ^{4}He/^{3}He thermochronometry results are shown in the supporting online material. Confidence intervals for each cooling path are approximately the same as that indicated by the difference between the red and blue curves in Fig. 2.

Figure 3 shows a set of cooling paths for four apatite samples collected from the western wall of the valley (Fig. 1) along with the solution for 01MR-59. All of the ^{4}He/^{3}He thermochronometry results (*18*) support the cooling history inferred from 01MR-59 and suggest that samples collected deep within the Klinaklini valley (at present elevations ≤2000 m) experienced rapid cooling, starting ~1.8 Ma. The four samples from the western wall require an earlier period of slower cooling (~20°C/10^6 years), between 5 and 2 Ma, and the two highest samples suggest even slower cooling before 5 Ma. As expected, the data require that samples at higher elevations were at lower temperatures, and therefore closer to the paleo-surface, as the Klinaklini valley deepened.

For instance, the data require that by 1.8 Ma, sample TEKI-23 was already at temperatures <20°C, and so was located very near the paleo-surface. Therefore, at that location, much less erosion occurred since 1.8 Ma than in the bottom of the valley. The present elevation of TEKI-23 is ~2100 m above sea level and ~1900 m above sample 01MR-59. The difference in elevation between TEKI-23 and 01MR-59 is in excellent agreement with the minimum amount of erosion inferred solely from 01MR-59. Intense glacial erosion ~1.8 Ma greatly deepened the Klinaklini valley and enhanced topographic relief between the locations of these two samples, although the region's relief before 1.8 Ma cannot be quantified solely from this data set. Further, because TEKI-38 is located at lower elevation than 01MR-59 yet was at lower temperatures, the comparative ^{4}He/^{3}He thermochronometry of these samples implies that glacial valley widening progressed toward the east.

Our results indicate acceleration in rock cooling and erosion rates at a time when widespread glaciation was active in North America, but nearly 900,000 years after the onset of Northern Hemisphere glaciation (*25*). We find that between 1.8 and 1.4 Ma, glacial erosion rates in the Klinaklini valley were significantly higher (by a factor of ≥6) than erosion rates before 1.8 Ma (between ~5 and 1.8 Ma), which more likely involved fluvial processes. The coincidence of this event with other erosion and climate events occurring in both the Northern and Southern hemispheres between 1.9 and 1.7 Ma (*26*–*29*, *32*, *33*) suggests that the intense erosion may be related to a global transition to increased climate variability at that time (*26*, *33*, *34*). This supports the notion that transitions out of periods of climate stability to high-frequency changes in temperature and precipitation enhance erosion by preventing fluvial and glacial systems from establishing new equilibrium states (*34*).

Although glacier ice likely existed within major valleys during more recent glaciations (i.e., after 1.4 Ma), ^{4}He/^{3}He thermochronometry indicates that most of the present relief of the Klinaklini valley developed shortly after continental ice sheets did, and that recent glacial advances resulted in considerably less net erosion within preexisting valleys. Thermochronometric evidence from the northern Coast Mountains revealed an average erosion rate of only 0.22 mm/year between 10 and 4 Ma and suggested a substantial increase in exhumation rate sometime after 4 Ma (*9*). If representative of the entire range, the Klinaklini data set suggests that the Coast Mountains experienced a major topographic modification after 2 Ma.

References and Notes

1. S. H. Brocklehurst, K. X. Whipple, *Geomorphology* **42**, 1 (2002).
2. D. R. Montgomery, *Geology* **30**, 1047 (2002).
3. N. Brozovic, D. W. Burbank, A. J. Meigs, *Science* **276**, 571 (1997).
4. P. Molnar, P. England, *Nature* **346**, 29 (1990).
5. B. Hallet, L. Hunter, J. Bogen, *Global Planet. Change* **12**, 213 (1996).
6. N. F. Humphrey, C. F. Raymond, *J. Glaciol.* **40**, 539 (1994).
7. E. E. Small, R. S. Anderson, *Geology* **26**, 123 (1998).
8. J. A. Spotila, J. T. Buscher, A. J. Meigs, P. W. Reiners, *Geology* **32**, 501 (2004).
9. K. A. Farley, M. E. Rusmore, S. W. Bogue, *Geology* **29**, 99 (2001).
10. R. B. Alley, D. E. Lawson, G. J. Larson, E. B. Evenson, G. S. Baker, *Nature* **424**, 758 (2003).
11. R. S. Anderson *et al.*, *J. Geophys. Res.* **109**, F03005 (2004).
12. J. H. Tomkin, J. Braun, *Am. J. Sci.* **302**, 169 (2002).
13. D. L. Shuster, K. A. Farley, *Earth Planet. Sci. Lett.* **217**, 1 (2004).
14. T. A. Ehlers, K. A. Farley, *Earth Planet. Sci. Lett.* **206**, 1 (2003).
15. K. A. Farley, in *Reviews in Mineralogy and Geochemistry: Noble Gases in Geochemistry and Cosmochemistry*, D. Porcelli, C. J. Ballentine, R. Wieler, Eds. (Mineralogical Society of America, Washington, DC, 2002), vol. 47, pp. 819–844.
16. D. L. Shuster, K. A. Farley, J. M. Sisterson, D. S. Burnett, *Earth Planet. Sci. Lett.* **217**, 19 (2004).
17. Separated populations (~mg) of apatites were irradiated with a 220-MeV proton beam generated by isochronous cyclotron acceleration. A fluence of ~10^{15} protons/cm^2 induced a uniformly distributed (*16*) ^{3}He concentration of ~10^8 atoms/mg. After irradiation, the dimensions of ≤20 whole, euhedral, similarly sized, inclusion-free crystals were measured, and the grains were loaded onto a thermocouple in copper foil under vacuum (*35*). Each sample was sequentially heated to a set temperature to ±2°C for a prescribed time [typically a few hours (*24*)], as previously described (*16*, *35*, *36*). After each heating step, the evolved ^{3}He abundance and ^{4}He/^{3}He ratio were measured by sector field mass spectrometry with mass resolution sufficient to resolve ^{3}He from HD. A correction for blank and proton-induced ^{4}He (proton-induced ^{4}He/^{3}He ~ 10) was applied to each measurement. Single grain (U-Th)/He ages were determined on nonirradiated samples by using conventional techniques (*15*). Uncertainties on (U-Th)/He ages were estimated from the reproducibility of replicated analyses, and uncertainties on ^{4}He/^{3}He were dominated by and estimated from uncertainty in ^{4}He blank corrections.
18. Additional details of ^{4}He/^{3}He thermochronometry and complete data sets are available as supporting material on *Science* Online.
19. For instance, a sample that experienced slow cooling will have a diffusive ^{4}He distribution with low concentration near the grain's edge, resulting in gradually increasing ^{4}He/^{3}He ratios upon sequential degassing (*13*). Unlike conventional age-elevation relationships (*37*), the technique does not rely on the relative positions and cooling ages of other samples; each sample provides independent information on its cooling history. By combining the cooling paths of multiple samples (e.g., along a vertical or horizontal transect), the evolving three-dimensional thermal field at depth is revealed. For instance, major changes in the thermal field, e.g., associated with deep glacial incision, should be recorded in proximate samples.
20. R. R. Parrish, *Tectonics* **2**, 601 (1983).
21. P. B. O'Sullivan, R. R. Parrish, *Earth Planet. Sci. Lett.* **132**, 213 (1995).
22. J. J. Clague, in *Quaternary Geology of Canada and Greenland*, R. J. Fulton, Ed. (Geological Survey of Canada, Vancouver, 1989), pp. 17–96.
23. We assume that the helium diffusion kinetics measured in the laboratory between 175° and 295°C can be extrapolated to the longer time scales and lower temperatures encountered in nature.
24. K. A. Farley, R. A. Wolf, L. T. Silver, *Geochim. Cosmochim. Acta* **60**, 4223 (1996).
25. G. H. Haug, D. M. Sigman, R. Tiedemann, T. F. Pedersen, M. Sarnthein, *Nature* **401**, 779 (1999).
26. A. C. Ravelo, D. H. Andreasen, M. Lyle, A. O. Lyle, M. W. Wara, *Nature* **429**, 263 (2004).
27. B. C. Reynolds, S. C. Sherlock, S. P. Kelley, K. W. Burton, *Geology* **32**, 861 (2004).
28. B. L. Winter, C. M. Johnson, D. L. Clark, *Geochim. Cosmochim. Acta* **61**, 4181 (1997).
29. K. E. K. St.John, *The Sedimentary Record* **2**, 4 (2004).
30. R. Hyndman, *J. Geophys. Res.* **81**, 337 (1976).
31. T. J. Lewis, A. M. Jessop, A. S. Judge, *Can. J. Earth Sci.* **22**, 1262 (1985).
32. M. H. Trauth, M. A. Mastin, A. Deino, M. R. Strecker, *Science* **309**, 2051 (2005).
33. M. W. Wara, A. C. Ravelo, M. L. Delaney, *Science* **309**, 758 (2005).
34. P. Z. Zhang, P. Molnar, W. R. Downs, *Nature* **410**, 891 (2001).
35. K. Farley, P. Reiners, V. Nenow, *Anal. Chem.* **71**, 2059 (1999).
36. K. A. Farley, *J. Geophys. Res.* **105**, 2903 (2000).
37. M. A. House, B. P. Wernicke, K. A. Farley, *Nature* **396**, 66 (1998).
38. H. Fechtig, S. Kalbitzer, in *Potassium-Argon Dating*, O. A. Schaeffer, J. Zahringer, Eds. (Springer, Heidelberg, 1966), pp. 68–106.

39. We thank G. Woodsworth for assistance in sample collection and providing access to the Digital Elevation Model used in Fig. 1 through collaboration with the Geologic Survey of Canada. We also thank J. M. Sisterson for help with the proton irradiation, L. M. Hedges for help with sample preparation, and M. S. Densmore. This work was supported by NSF grants EAR-0408526 and 0309779.

Supporting Online Material

www.sciencemag.org/cgi/content/full/310/5754/1668/DC1
SOM Text
Figs. S1 to S5
Tables S1 to S5
References and Notes

8 August 2005; accepted 7 November 2005
10.1126/science.1118519

www.sciencemag.org/cgi/content/full/310/5754/1668/DC1

Supporting Online Material for

Rapid Glacial Erosion at 1.8 Ma Revealed by $^{4}He/^{3}He$ Thermochronometry

David L. Shuster,* Todd A. Ehlers, Margaret E. Rusmore, Kenneth A. Farley

*To whom correspondences should be addressed at Berkeley Geochronology Center, 2455 Ridge Road, Berkeley, CA 94709, USA. E-mail: dshuster@bgc.org

Published 9 December 2005, *Science* **310**, p1668 (2005)
DOI: 10.1126/science.1118519

This PDF file includes:

Supplementary Information for:
Shuster, D.L., T.A. Ehlers, M.E. Rusmore, and K.A. Farley (2005)
Rapid Glacial Erosion at 1.8 Ma Revealed by ^{4}He/^{3}He Thermochronometry, *Science*

Thermochronometry often involves the determination of a cooling age from parent and daughter abundances within an entire crystal or population of crystals (*1*). Complementary information exists in the spatial concentration distribution of the daughter within a single crystal. By combining a bulk cooling age with the spatial distribution of the daughter on the same sample, it is possible to place tight limits on the sample's time-temperature *(t-T)* path

This approach is applied to the (U-Th)/He system by introducing synthetic ^{3}He via proton irradiation (*2*). The attraction of the (U-Th)/He system is its sensitivity to uniquely low temperatures. For example, the nominal ^{4}He closure temperature (at 10^{o}C/Myr) for apatite is 60^{o}C (*3*). Therefore, significant diffusion of ^{4}He occurs at temperatures just slightly higher than those of Earth's surface.

In *^{4}He/^{3}He thermochronometry* (*4*), the natural spatial distribution of ^{4}He is constrained by stepwise degassing ^{4}He/^{3}He analysis of a sample containing synthetic, proton-induced ^{3}He. Since the distribution of the ^{3}He is spatially uniform (*2*), release fractions of proton-induced ^{3}He can be used to determine the helium diffusion kinetics (*5*) (e.g., Fig. S1-S4, panels (a)). Upon stepwise degassing, sequentially measured ^{4}He/^{3}He ratios constrain the natural ^{4}He distribution within an individual crystal or a small population of crystals. Evolution of the ^{4}He/^{3}He ratio reveals the distribution of radiogenic ^{4}He within a sample. For instance, a ^{4}He distribution solely resulting from α-ejection (*6*) (i.e., due to rapid cooling), will have relatively high ^{4}He/^{3}He ratios at the beginning of a degassing experiment. Conversely, a diffusive ^{4}He distribution resulting from gradual cooling will have low ^{4}He near the grain's edge and therefore low initial ^{4}He/^{3}He ratios which steadily rise over the course of an analysis (*4*). The ^{4}He/^{3}He ratios of the first ~40% of helium extracted over the course of an analysis contain the highest resolving power on the ^{4}He distribution (*4*). Note that the ^{4}He/^{3}He ratios measured toward the end of an experiment are often not useful for constraining the spatial distribution of ^{4}He in the sample, but must be incorporated when calculating the bulk ^{4}He/^{3}He ratio of a sample (*7*).

Together, the helium diffusion kinetics and the spatial distribution of ^{4}He can be used to constrain the sample's *t-T* path. To quantify a sample's thermal history from an observed radiometric age and an inferred spatial distribution of the daughter product is formally an ill posed problem: a set of *t-T* solutions can be constrained, although a single solution does not generally exist. The age and concentration profile together limit acceptable cooling paths.

As discussed in the main text, the ^{4}He/^{3}He results of 01MR-59 demand rapid cooling of at least 50^{o}C at between 1.8 Ma and 1.4 Ma. A cooling event of this magnitude should be recorded in proximate samples. Here, we use the ^{4}He/^{3}He results for samples (TEKI-38, TEKI-34, TEKI-30, and TEKI-23) collected along a nearly vertical profile to test this cooling model. The models presented below are an internally consistent set of solutions that have been bootstrapped from the 01MR-59 result. All models were constrained to a vertical geothermal gradient $\leq$ 30^{o}C/km. From this analysis, we find that all samples at elevation $\leq$ 2000 m support the occurrence of a rapid

cooling event at 1.8 ± 0.2 Ma. Together, the set of solutions places tight constraints on the thermal history of the valley.

Tables S1-S5 ^{4}He/^{3}He thermochronometry data tables for TEKI-38 (**S1**), TEKI-34 (**S2**), TEKI-30 (**S3**) and TEKI-23 (**S4**), and 01MR-59 (**S5**), respectively.

Figures S1-S5 ^{4}He/^{3}He thermochronometry for apatite samples TEKI-38 (**S1**), TEKI-34 (**S2**), TEKI-30 (**S3**), TEKI-23 (**S4**) and 01MR-59 (**S5**), respectively. **(a)** Arrhenius plots; circles are the diffusion coefficients, *D*, normalized to the diffusive length scale, *a*, calculated (*5*) from release fractions of proton-induced ^{3}He (*2*). Solid black line is the inferred helium diffusion kinetics for each sample used to construct models shown in (b,c), determined by linear regression of a subset array. Steps deviate from linearity above 300 ^{o}C due to a change in mechanism (*3*) which may not apply to lower temperatures relevant to our models and are therefore excluded from the regression. **(b)** Model *t-T* paths. Each of these models corresponds to the observed (U-Th)/He age for each sample, which is indicated in the lower panels. **(c)** Ratio evolution diagrams. Shown are measured isotope ratios for each release step, R_{step} (R=^{4}He/^{3}He), normalized to the bulk ratio R_{bulk}, plotted versus the cumulative ^{3}He release fraction, ΣF^3He. Each model shown in (c) corresponds to the *t-T* path in (b). Also shown for reference are two end-member ^{4}He distributions, i.e., the α-ejection only distribution (dashed line) and the steady-state distribution (dotted line) (*4*). Due to a change in diffusive mechanism at temperatures >300 ^{o}C which were used toward the end of these experiments (*3*), and because the initially extracted gas contains the highest resolving power on the spatial distribution of ^{4}He (*4*), models were matched only to values of ΣF^3He ≤ 0.4. For these reasons, data collected for ΣF^3He > 0.6 do not well represent the spatial distribution of ^{4}He (*7*) and were not considered in our modeling, although all points were used to calculate the bulk ^{4}He/^{3}He ratio of each sample. Error bars are specified by a vertical line through each point. Data scatter and uncertainty is largely a function of the absolute ^{4}He abundance in each sample and the corresponding magnitude of ^{4}He blank corrections. For instance, TEKI-38 contains a ^{4}He abundance that is 7% of that of TEKI-23.

References

1. M. H. Dodson, *Contributions to Mineralogy and Petrology* **40**, 259 (1973).
2. D. L. Shuster, K. A. Farley, J. M. Sisterson, D. S. Burnett, *Earth and Planetary Science Letters* **217**, 19 (2004).
3. K. A. Farley, *Journal of Geophysical Research* **105**, 2903 (2000).
4. D. L. Shuster, K. A. Farley, *Earth and Planetary Science Letters* **217**, 1 (2004).
5. H. Fechtig, S. Kalbitzer, in *Potassium-Argon Dating* O. A. Schaeffer, J. Zahringer, Eds. (Springer, Heidelberg, 1966) pp. 68-106.
6. K. A. Farley, R. A. Wolf, L. T. Silver, *Geochimica et Cosmochimica Acta* **60**, 4223 (1996).
7. D. L. Shuster, K. A. Farley, in *Low-Temperature Thermochronology: Techniques, Interpretations and Applications* P. W. Reiners, T. A. Ehlers, Eds. (2005), vol. 58, pp. 181-203.

Table S1: TEKI-38

Step	T (oC)	time (hr)	^{3}He (atoms/10^6)	R_{step}/R_{bulk}*	(+/-)
1	150	0.50	0.09	b.d.	b.d.
2	150	0.75	0.06	b.d.	b.d.
3	150	1.00	0.05	b.d.	b.d.
4	175	0.75	0.16	b.d.	b.d.
5	175	1.25	0.18	b.d.	b.d.
6	200	0.75	0.40	b.d.	b.d.
7	200	1.25	0.46	b.d.	b.d.
8	225	0.50	0.60	0.29	0.47
9	225	1.25	1.09	0.42	0.27
10	250	0.75	1.74	0.27	0.17
11	250	1.25	1.81	0.58	0.16
12	240	1.25	0.97	0.53	0.30
13	230	1.50	0.58	b.d.	b.d.
14	220	2.00	0.35	b.d.	b.d.
15	235	2.50	0.89	b.d.	b.d.
16	275	0.75	2.48	0.38	0.12
17	275	1.25	2.55	0.59	0.12
18	300	0.75	3.91	0.50	0.08
19	300	1.25	4.63	0.68	0.07
20	325	0.50	4.57	0.55	0.07
21	325	1.25	8.44	0.69	0.05
22	350	1.25	13.15	0.87	0.03
23	375	0.50	10.37	0.81	0.04
24	425	0.50	22.84	1.03	0.02
25	475	0.50	29.55	1.15	0.02
26	525	0.50	21.76	1.26	0.03
27	575	0.50	5.81	1.51	0.06
28	600	0.50	1.37	1.92	0.22
29	600	1.00	0.49	3.68	0.59
30	600	2.00	0.15	9.66	1.94
31	1200	0.10	0.86	1.73	0.27
Total			142.36		

*R = ^{4}He/^{3}He, R_{bulk} = 26

b.d. is below detection limit

Table S2: TEKI-34

Step	T (oC)	time (hr)	^{3}He (atoms/10^6)	R_{step}/R_{bulk}*	(+/-)
1	150	0.50	0.12	b.d	b.d
2	150	0.75	0.08	b.d	b.d
3	150	1.00	0.07	b.d	b.d
4	175	0.75	0.24	b.d	b.d
5	175	1.25	0.27	0.37	0.80
6	200	0.75	0.64	0.10	0.34
7	200	1.25	0.72	0.25	0.30
8	225	0.50	0.83	0.26	0.27
9	225	1.25	1.61	0.47	0.14
10	250	0.75	3.32	0.36	0.07
11	250	1.25	3.74	0.52	0.07
12	240	1.25	1.90	0.49	0.12
13	230	1.50	0.88	0.46	0.25
14	220	2.00	0.61	0.46	0.37
15	235	2.50	1.72	0.49	0.14
16	275	0.75	6.03	0.57	0.05
17	275	1.25	6.18	0.63	0.05
18	300	0.75	9.10	0.67	0.03
19	300	1.25	6.32	0.73	0.04
20	325	0.50	5.70	0.69	0.05
21	325	1.25	10.56	0.79	0.03
22	350	1.25	18.14	0.86	0.02
23	375	0.50	12.58	0.97	0.03
24	425	0.50	36.59	1.01	0.02
25	475	0.50	57.06	1.10	0.01
26	525	0.50	53.67	1.21	0.01
27	575	0.50	21.78	1.23	0.02
28	600	0.50	3.31	1.65	0.07
29	600	1.00	1.29	2.14	0.17
30	600	2.00	1.13	2.44	0.19
31	1200	0.10	2.99	0.45	0.09
Total			269.21		

*R = ^{4}He/^{3}He, R_{bulk} = 52

b.d. is below detection limit

Table S3: TEKI-30

Step	T (oC)	time (hr)	^{3}He (atoms/10^6)	R_{step}/R_{bulk}*	(+/-)
1	150	0.50	0.08	b.d.	b.d.
2	150	0.75	0.04	b.d.	b.d.
3	150	1.00	0.06	b.d.	b.d.
4	175	0.75	0.14	b.d.	b.d.
5	175	1.25	0.15	b.d.	b.d.
6	200	0.75	0.35	0.18	0.64
7	200	1.25	0.36	0.22	0.63
8	225	0.50	0.50	0.19	0.46
9	225	1.25	0.84	0.34	0.29
10	250	0.75	1.53	0.38	0.17
11	250	1.25	1.63	0.43	0.16
12	240	1.25	0.67	0.38	0.36
13	230	1.50	0.47	0.42	0.50
14	220	2.00	0.32	0.26	0.73
15	235	2.50	0.76	0.58	0.32
16	275	0.75	1.65	0.45	0.15
17	275	1.25	2.31	0.61	0.11
18	300	0.75	3.31	0.64	0.08
19	300	1.25	4.29	0.71	0.06
20	325	0.50	3.59	0.71	0.07
21	325	1.25	6.87	0.86	0.04
22	350	1.25	11.87	0.91	0.03
23	375	0.50	7.95	0.93	0.04
24	425	0.50	22.34	1.06	0.02
25	475	0.50	30.99	1.19	0.02
26	525	0.50	26.62	1.15	0.02
27	575	0.50	8.58	1.13	0.04
28	600	0.50	1.16	1.36	0.22
29	600	1.00	0.77	1.45	0.32
30	600	2.00	0.55	2.16	0.45
31	1200	0.10	1.63	1.21	0.06
Total			142.38		

*R = ^{4}He/^{3}He, R_{bulk} = 96

b.d. is below detection limit

Table S4: TEKI-23

Step	T (oC)	time (hr)	^{3}He (atoms/10^6)	R_{step}/R_{bulk}*	(+/-)
1	150	0.50	0.10	b.d.	b.d.
2	150	0.75	0.10	b.d.	b.d.
3	150	1.00	0.19	b.d.	b.d.
4	175	0.75	0.38	b.d.	b.d.
5	175	1.25	0.39	b.d.	b.d.
6	200	0.75	0.83	b.d.	b.d.
7	200	1.25	0.88	0.35	0.16
8	225	0.50	1.26	0.34	0.12
9	225	1.25	2.15	0.38	0.07
10	250	0.75	2.92	0.45	0.05
11	250	1.25	3.61	0.49	0.04
12	240	1.25	1.65	0.54	0.09
13	230	1.50	1.05	0.55	0.15
14	220	2.00	0.81	0.51	0.19
15	235	2.50	1.95	0.59	0.08
16	275	0.75	3.48	0.56	0.05
17	275	1.25	4.45	0.61	0.04
18	300	0.75	6.70	0.64	0.03
19	300	1.25	7.47	0.71	0.03
20	325	0.50	5.97	0.75	0.03
21	325	1.25	11.01	0.78	0.02
22	350	1.25	18.16	0.89	0.02
23	375	0.50	10.38	0.96	0.02
24	425	0.50	28.16	1.02	0.01
25	475	0.50	36.15	1.12	0.01
26	525	0.50	28.21	1.17	0.01
27	575	0.50	17.64	1.14	0.01
28	600	0.50	9.52	1.13	0.02
29	600	1.00	7.68	1.13	0.03
30	600	2.00	5.24	1.36	0.02
31	1200	0.10	6.56	1.35	0.02
Total			225.04		

*R = ^{4}He/^{3}He, R_{bulk} = 356

b.d. is below detection limit

Table S5: Apatite 01mr-59

Step	T (oC)	time (hr)	^{3}He (atoms/10^6)	R_{step}/R_{bulk}*	(+/-)
1	175	0.75	0.35	0.134	0.051
2	175	1.00	0.17	0.183	0.076
3	175	3.00	0.21	0.345	0.127
4	188	1.00	0.13	0.458	0.165
5	188	1.50	0.17	0.423	0.147
6	188	2.00	0.16	0.268	0.108
7	200	0.50	0.08	0.275	0.118
8	200	1.00	0.16	0.368	0.134
9	200	1.50	0.22	0.379	0.126
10	200	2.00	0.27	0.563	0.153
11	225	0.50	0.32	0.663	0.135
12	225	2.00	0.80	0.537	0.080
13	225	2.00	0.73	0.551	0.086
14	250	0.50	0.69	0.724	0.082
15	250	1.00	1.09	0.562	0.057
16	250	2.00	1.51	0.580	0.050
17	275	0.50	1.22	0.615	0.050
18	275	1.00	1.97	0.671	0.036
19	275	2.00	2.87	0.682	0.029
20	295	0.50	1.53	0.691	0.042
21	295	1.00	2.52	0.732	0.029
22	295	2.00	3.80	1.003	0.023
23	305	0.50	1.15	0.819	0.054
24	305	1.00	2.23	0.802	0.032
25	305	1.25	2.30	0.805	0.033
26	305	2.00	3.00	0.834	0.028
27	315	0.50	1.04	0.877	0.060
28	315	1.00	1.91	0.874	0.038
29	315	1.25	1.89	0.912	0.039
30	315	1.75	2.56	0.908	0.032
31	325	0.50	1.01	0.928	0.062
32	325	1.50	2.15	0.981	0.036
33	325	1.50	2.14	0.947	0.036
34	325	2.00	2.30	0.970	0.036
35	335	0.50	0.87	0.971	0.071
36	335	1.00	1.57	0.979	0.066
37	335	1.50	2.00	1.044	0.073
38	335	2.00	2.41	1.121	0.078
39	345	1.00	1.69	1.048	0.082
40	350	0.50	1.00	1.003	0.094
41	360	0.50	1.39	0.973	0.071
42	360	1.00	2.16	1.044	0.034
43	370	0.50	1.58	1.000	0.042
44	370	1.00	2.46	1.026	0.030
45	380	0.50	1.43	1.052	0.046
46	390	0.50	1.73	1.067	0.039
47	400	1.00	3.14	1.307	0.076
48	425	0.50	2.80	1.127	0.025
49	450	0.25	2.07	1.185	0.032
50	450	0.25	1.94	1.111	0.034
51	475	0.25	2.37	1.120	0.028
52	475	0.25	1.46	1.151	0.044
53	475	0.50	1.61	1.362	0.042
54	475	0.50	0.89	1.445	0.073
55	500	0.25	0.62	1.467	0.097
56	500	0.25	0.34	1.593	0.162
57	550	0.50	0.71	1.693	0.156
58	550	0.75	0.45	2.602	0.363
59	550	1.00	0.43	1.895	0.339
60	550	3.00	0.47	1.538	0.317
61	525	5.00	0.72	1.619	0.260
62	525	5.00	0.62	1.330	0.268
63	600	5.00	0.97	1.535	0.208
64	600	5.00	0.88	1.615	0.228
65	620	5.00	0.72	1.663	0.263
66	1200	0.10	1.74	1.660	0.271
Total			89.89		

*R = ^{4}He/^{3}He, R_{bulk} = 236

Shuster, Ehlers, Rusmore, Farley (2005)
Figure S1

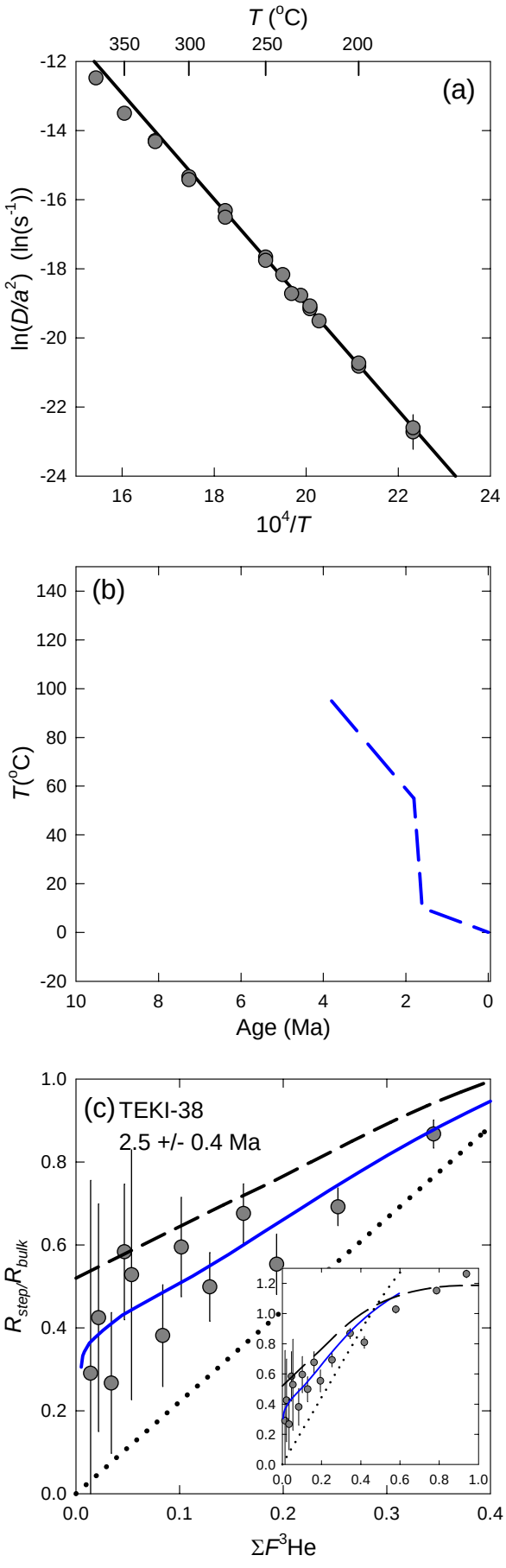

Shuster, Ehlers, Rusmore, Farley (2005)
Figure S2

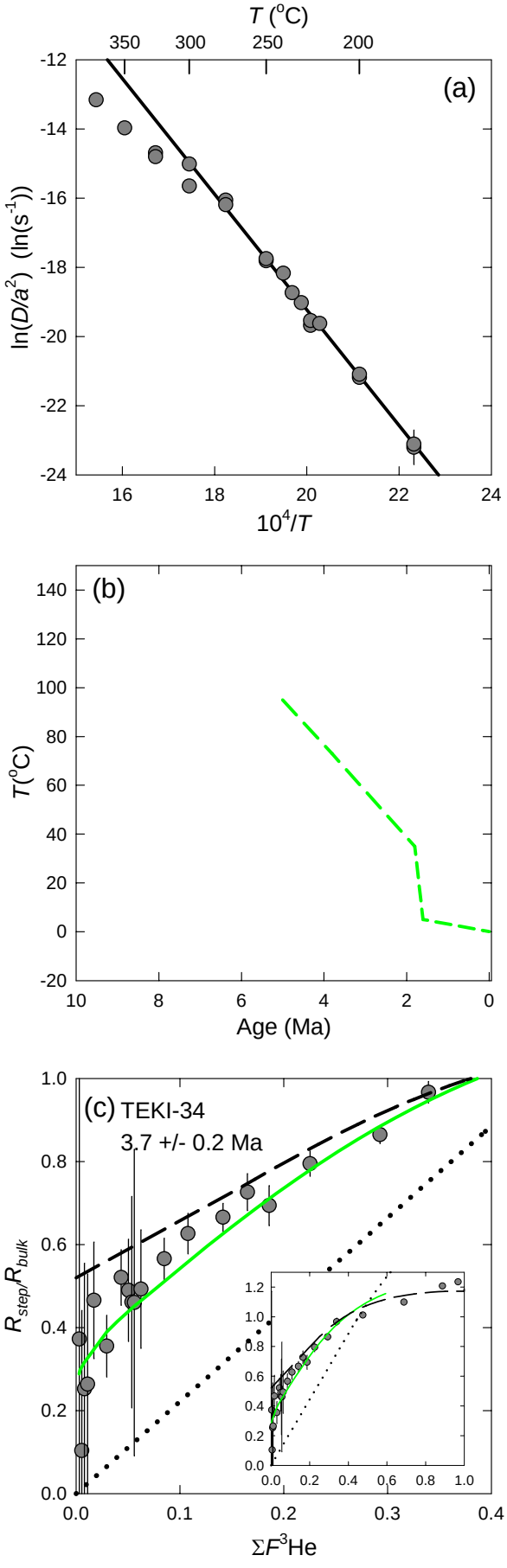

Shuster, Ehlers, Rusmore, Farley (2005)
Figure S3

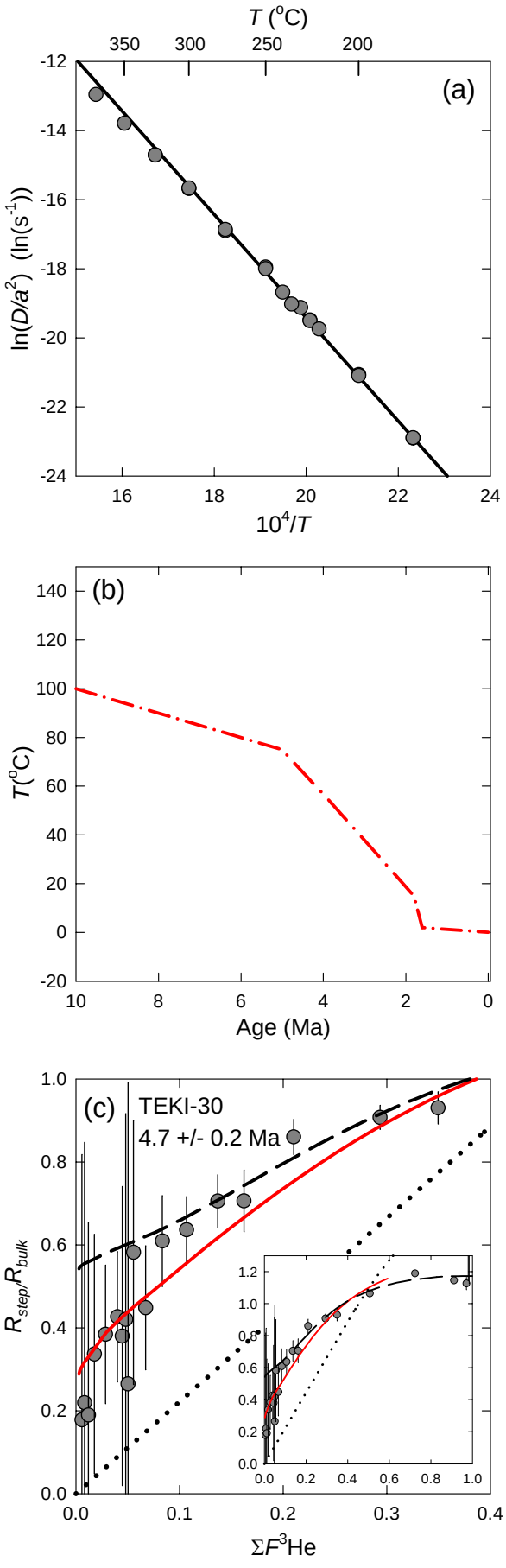

TEKI-30

4.7 +/- 0.2 Ma

Shuster, Ehlers, Rusmore, Farley (2005)
Figure S4

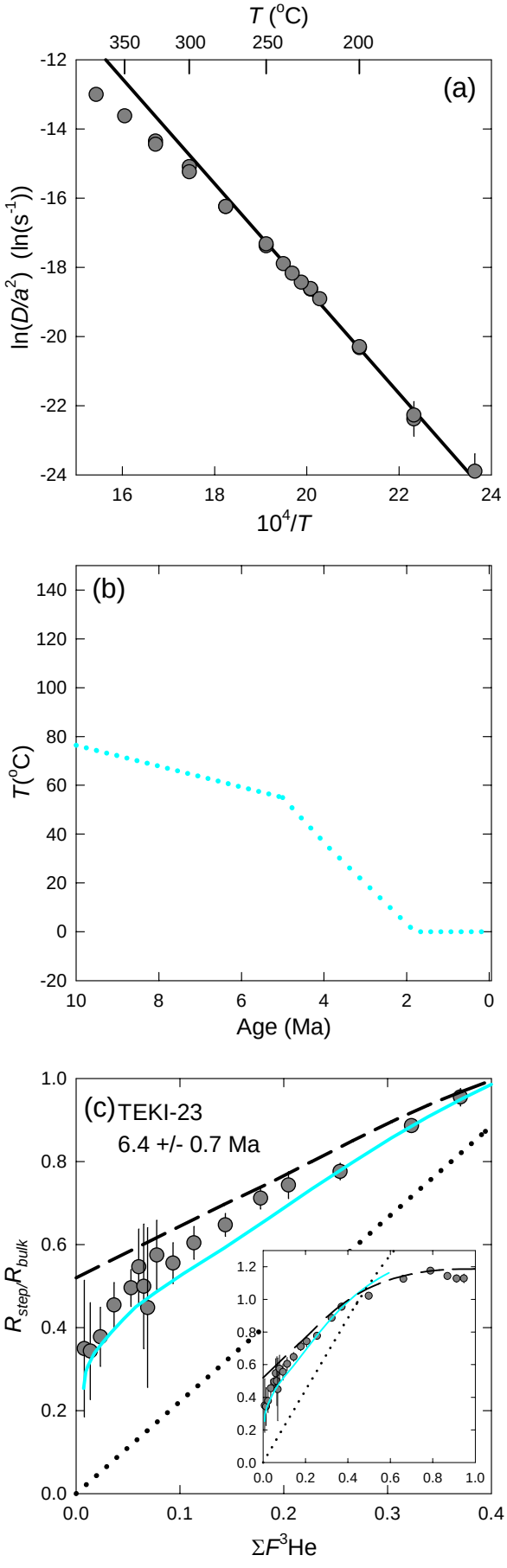

Shuster, Ehlers, Rusmore, Farley (2005)
Figure S5